Optimizing phenol-modified hyaluronic acid for designing shape-maintaining biofabricated hydrogel scaffolds in soft tissue engineering

Julia Simińska-Stanny[a,b], Feza Hachemi[a,c], Gianina Dodi[d], Florina D. Cojocaru[d], Ioannis Gardikiotis[e], Daria Podstawczyk[b], Christine Delporte[f], Guohua Jiang[g], Lei Nie[a,h], *Amin Shavandi[a*]

[a] Université libre de Bruxelles (ULB), École polytechnique de Bruxelles, 3BIO-BioMatter, Avenue F.D. Roosevelt, 50 - CP 165/61, 1050 Brussels, Belgium

[b] Department of Process Engineering and Technology of Polymer and Carbon Materials, Faculty of Chemistry, Wroclaw University of Science and Technology, Norwida 4/6, 50-373 Wroclaw, Poland

[c] Université Paris Saclay, Polytech Paris Saclay, Rue Louis de Broglie, 91400 Orsay, France

[d] Faculty of Medical Bioengineering, Grigore T. Popa, University of Medicine and Pharmacy of Iasi, Romania

[e] Advanced Research and Development Center for Experimental Medicine (CEMEX), Grigore T. Popa, University of Medicine and Pharmacy of Iasi, Romania

[f] Université libre de Bruxelles (ULB), Faculté de Médecine, Campus Erasme - CP 611, Laboratory of Pathophysiological and Nutritional Biochemistry, Route de Lennik, 808, 1070 Bruxelles,

[g] School of Materials Science and Engineering, Zhejiang Sci-Tech University, Hangzhou, ChinaInternational Scientific and Technological Cooperation Base of Intelligent Biomaterials and Functional Fibers, Zhejiang Sci-Tech University, Hangzhou, China

[h] College of Life Science, Xinyang Normal University, Xinyang, China

*Corresponding author: Amin Shavandi (amin.shavandi@ulb.be)

1. Introduction

Developing a biomaterial ink suitable for use in the creation of a 3D model of soft tissues such as the salivary gland (SG) tissue which is compatible with epithelial organs is one of the principal challenges [1]. Matrigel® is a frequently used hydrogel biomaterial for SG tissue engineering but its animal origin limits clinical use [2]. Hyaluronic acid (HA)-based hydrogels, collagen, fibrin, fibronectin, and silk fibroin protein-hydrogels have been explored as alternatives for 3D culture and promoting SG epithelial cell growth and differentiation [3]. However, most studies have only examined cellular functionality in simple 3D cell cultures, and there is still a need for biomaterial inks that are biocompatible, degrade with 3 to 5 weeks, have mechanical properties similar to SG basement membrane, and support branching morphogenesis for regeneration [1, 2].

HA, a crucial component of the extracellular matrix (ECM), provides viscoelasticity and mechanical stability to the tissue, and regulates cellular functions such as adhesion, migration, proliferation, and differentiation by interacting with cellular receptors [4]. Its activity in biological responses can vary with HA molecular weight and was shown to impact its antimicrobial activity [5]. HA has also been shown to promote ECM production and stimulate synthesis of type II collagen [6], in a form of particles HA with conductive PEDOT (Poly(3,4-ethylenedioxythiophene)) proved to be an efficient stabilizer for conductive and biological applications [7]. Lee et al. [8] showed that HA is a crucial GAG for the SG organogenesis process, additionally some recent studies explored the potential of HA as a nanocoating in cell transplantations [9]. Despite multiple benefits the low viscosity of HA limits its versatility for 3D printing [10]. However, it is possible to enzymatically form HA hydrogel by introducing phenolic groups such as tyramine into the

HA backbone using horseradish peroxidase (HRP) and oxidizing agents allowing for enzymatic as well as a photo-gelation of the modified HA [11]. Gelatin is a cost-effective and widely available hydrogel material, commonly modified by methacrylation to create a cross-linkable gelatin hydrogel. GelMA hydrogels are biocompatible, able to be degraded by matrix metalloproteinases (MMPs) and reported as good materials for tissue engineering purposes [12-14]. However, their use for 3D bioprinting of SG models has yet to be investigated. To overcome limitations such as low stiffness and short degradation time, researchers have investigated multicomponent composite inks and photo-assisted crosslinking systems using visible light sources such as a combination of riboflavin and sodium persulfate [11, 13, 15].

To address the challenges of finding a versatile printable material for the creation of the 3D model, we employed a design of experiment (DoE) to determine the relationship between the ink composition and printing performance of the formulated inks. DoE can facilitate the efficient development of biomaterial formulations for 3D printing through systematic manipulation of variables [16] to enhance efficiency and improve prediction of outcomes. DoE allows multiple factors to be varied simultaneously, significantly reducing the number of experiment while still permitting analysis of the parameters of individual effects to be separated using statistical analysis revealing the key dependencies of different variables for particular responses [16-18]. Despite numerous advantages, DoE was rarely applied to optimize ink formulation for 3D printing [16, 19, 20]. Many studies emphasized the need of ink and printing process optimization; however, they are based on image evaluation without quantification [21]. A full-factorial design employed by Trachtenberg et all., facilitated the investigation of the impact of four factors on the fiber extrusion [18]. The effect of polymer concentration (alginate, nanocellulose, and fibrinogen on print durability and cell viability was investigated in a study by Hegab et al. that used DoE to

maximize durability of printed tissue over time while maintaining cell viability and bioink extrudability [16].

Central Composite Design (CCD) and Box Behnken design (BBD) are commonly used designs providing often comparable results [22]. We employed BBD to reduce the number of experiments by eliminating experiments required for extreme conditions as in CCD [22, 23]. In the case of ink formulations extreme conditions do not bring crucial insight in terms of printability and ink formulation as those points remain nonprintable either due to too low or too high viscosity of the material. Additionally BBD was reported to bring similar efficiency for the quadratic regression modeling approach versus the FFD in a study by Kechagias et all., investigating the ultimate tensile strength in material extrusion 3D printing [22].

Here, with the help of a DoE approach – Box Behnken design, we designed optimized dually crosslinked 3D printable inks based on GelMA and tyramine-modified HA. We explored the use of visible light and enzymatic crosslinking to tailor dual-stage crosslinking materials, specifically by combining GelMA and HA with methylcellulose (MC) as a rheological modifier to design a soft hydrogel mimicking elastic behavior of SG. A Box Behnken design was used to investigate the relationship between the ink composition and printing performance and finally the best printable ink formulation was further evaluated in various mechanical and biological tests.

2. Materials and methods

2.1. Materials

Gelatin from porcine skin (type A, gel strength 300 bloom, BioReagent, 70-90% of protein), horseradish peroxidase (HRP, ~150 U/mg), phosphate-buffered saline (PBS),

methacrylic anhydride (MAA, 94%), sodium persulfate (SPS, ≥94%) were purchased from Sigma-Aldrich (St. Louis, MO, USA). Tyramine hydrochloride (Tyr, >95%) was obtained from BIOSYNTH (Berkshire, Massachusetts, USA). 4-(4,6-Dimethoxy-1,3,5-triazine-2-yl)-4-methylmorpholinium chloride (DMTMM, >95%), deuterium oxide (D_2O, 99.9%) were purchased from Tokyo Chemical Industry (TCI, Tokyo, Japan), hydrogen peroxide (H_2O_2, EMSURE®, 30%) was purchased from Millipore Corporation (Germany). HA (molecular weight 300 kDa, verified via gel permeation chromatography (GPC) was obtained from Xi'an JKA Biotech Co., Ltd. (Xi'an, China). Riboflavin 5'-monophosphate sodium salt (73-79 % fluorometric) was purchased from J&K (Pforzheim, Germany) and Dulbecco's Modified Eagle Medium (DMEM) from PAN Biotech (Aidenbach, Germany). Methylcellulose (MC, Metolose SM-4000 mPa·s, substitution with methyl groups 27.5-31.5 %, food-grade) was kindly provided by Shinetsu Chemical Co., Japan). SV-40 immortalized human salivary gland cells with the acinar phenotype (NS-SV-AC) were kindly provided by Professor Azuma [24]. The mounting reagent came from IBIDI (Gräfelfing, Germany). Trypsin/EDTA, Glutamine, Penicillin-streptomycin, FBS, DMEM with high glucose, Ham-F12, and Ethidium homodimer were purchased from ThermoFisher Scientific (Waltham, MA, USA).

2.2. Materials modification

Methacrylated gelatin (GelMA) and tyramine conjugated HA (HA-Tyr) were obtained using the previously described protocols [12, 13] for GelMA and [25] for HA-Tyr (S1.1).

To verify the modifications of gelatin and HA and to determine the substitution degree of synthesized polymeric compounds (GelMA, HA-Tyr), 1H NMR analyses were performed at 25 °C using a spectrometer (JEOL JNM-ECZ600R/S3) with D_2O as the solvent. The 1H NMR spectra for 10 mg/mL polymers in D_2O were processed using MestReNova x64

software. The fraction of lysine groups from gelatin that reacted with MAA gave the information about methacrylation degree of gelatin [12, 14]. The HA substitution degree was determined based on amine groups that reacted with tyramine. The percentage of functional groups per repetition unit of methacrylated gelatin and phenolated HA was determined by the ratio of the integrals of the peak corresponding to the modification and the signal of the polymer backbone. The percentage of functional groups was calculated by dividing the sum of integrals of the functional group signals by the integrals of the signals originating from the polymer backbone as denoted in Equation 1 and 2 for GelMA and HA-Tyr respectively [12, 26].

$$Methacrylation\ degree\ (\%) = \frac{integral\ of\ GelMA\ lysine\ signal}{integral\ of\ Gelatin\ lysine\ signal} \cdot 100\% \qquad (Eq.1)$$

$$Tyramine\ substitution\ (\%) = \frac{integral\ of\ aromatic\ signal\ at\ 6.85\ ppm}{integral\ of\ N-acetylglucosamine\ signal\ of\ HA} \cdot 100\% \qquad (Eq.2)$$

ATR-FTIR interferograms were determined experimentally using an FTIR spectroscopy device (Nicolet Summit PRO, Thermo Fisher Scientific, USA) within a scan range of 4000–400 cm^{-1} and a resolution of 1 cm−1.

2.3. Formulation of the biomaterial inks

A series of inks based on GelMA, HA-Tyr and MC were prepared at 37° C limiting the access of the light. Polymer ratios in the blend were determined based on the design of the experiment, to find an optimal formulation for the 3D printing. Briefly, an amber glass vial filled with DMEM (V = 4.4 mL) was placed on a magnetic stirrer at 400 RPM, 37° C. A defined quantity of GelMA and HA-Tyr were added and kept under stirring, until complete dissolution. Subsequently, the appropriate amount of MC was added. Preliminary

crosslinking was induced by HRP addition (50 μL, to a final concentration of 2 U/mL), followed by drop-wise addition of H_2O_2 (50 μL, to a final concentration of 0.2 mM). The solution was mixed for 5 min to uniformly combine the reagents. Next, 250 μL of SPS - DMEM solution (to a final concentration of 20 mM) and 250 μL of RB - DMEM solution (to a final concentration of 2 mM) were introduced and mixed for 3 min. When a uniform suspension was obtained, the formulation was cooled down at room temperature and used for experiments or stored in a fridge (4 °C), away from light.

Throughout our study to enzymatically (preliminarily) crosslinked material, we refer as ink.

2.4. Hydrogel formation and 3D printing

Prior to the printing process, the warm ink (37 ^{o}C) was transferred into a 10 mL UV-shielded syringe to avoid the formation of air bubbles. For 3D printing, the ink was pneumatically extruded onto a Petri dish using a 3D printer - GeSim BioScaffolder 3.2 (Germany) through the 22G, 25G, or 27G nozzle at a pressure ranging from 40 to 100 kPa and speed of 5–7 mm/s according to a previously set geometry. Fabricated 3D scaffolds were cured to obtain stable hydrogels. The crosslinking was performed using the visible light source (Dymax, VisiCure – 405 nm, Mavom, Belgium) for 1 min [27].

To obtain hydrogel materials via molding the warm ink was transferred to the mold (dimensions of the mold used are described in S1.2 corresponding to mechanical measurements) using pipette or a spatula, following that a crosslinking step was performed, similarly as for a 3D-printed sample. Following the photocuring hydrogels were immediately used for tests or immersed in DMEM to avoid drying. Throughout our study, we refer to the dually crosslinked material as hydrogel.

Crosslinking density (mol/m^3) was determined according to Equation 3 [20] before and following the primary (enzymatic crosslinking) and secondary crosslinking (photo-curing) procedures.

$$n_e = \frac{G_e}{RT} \qquad (Eq. 3)$$

Where, G_e is the average value of storage modulus (G') from the linear region of the oscillatory frequency sweep measurements, R the ideal gas constant $\left[\frac{m^3 \cdot Pa}{K \cdot mol}\right]$ and T the absolute temperature [K].

We used the parameter optimization index (POI) as an useful tool that allows to adjust the accuracy of the print and at the same time minimizing theoretical shear stress (TSS), crucial for the ink to be successfully used for cell encapsulation and bioprinting [28, 29]. POI was calculated by employing Equation 4.

$$POI = \frac{1}{D_l \cdot n \cdot p} \qquad (Eq. 4)$$

Where, D_l [mm] is a printed line thickness, n [G] nozzle gauge size and p printing pressure.

To determine suitable printing parameters for the chosen formulation of biomaterial ink we printed 30 mm lines using straight cylindrical nozzles of 25G, 27G and 30G, with printing speeds of 5 - 7 mm/s and pressures of 40 - 100 kPa. All printouts were photographed to determine line thickness (by ImageJ software).

2.5. Optimization of hydrogel composition

A biomaterial ink may exhibit suitable rheological properties in terms of shear thinning and viscoelastic properties but it cannot always be successfully transformed into a stable

scaffold employing 3D printing [20]. To determine the influence of the hydrogel components on printability performance, a DoE was performed according to a Box Behnken Design with a concentration range of GelMA from 3 % (w/v) to 7 % (w/v), HA-Tyr from 1 % (w/v) to 3 % (w/v) and MC from 3 % (w/v) to 6 % (w/v) (Figure 1). Formulations determined in DoE were subsequently printed into grid patterns and followed by the determination of grid printability – P_g (Equation 4). Coded values requiring experimental evaluation and statistical analysis (ANOVA) of the experimental results were obtained using the Design Expert® software in 15 experimental runs including 3 replications for central points.

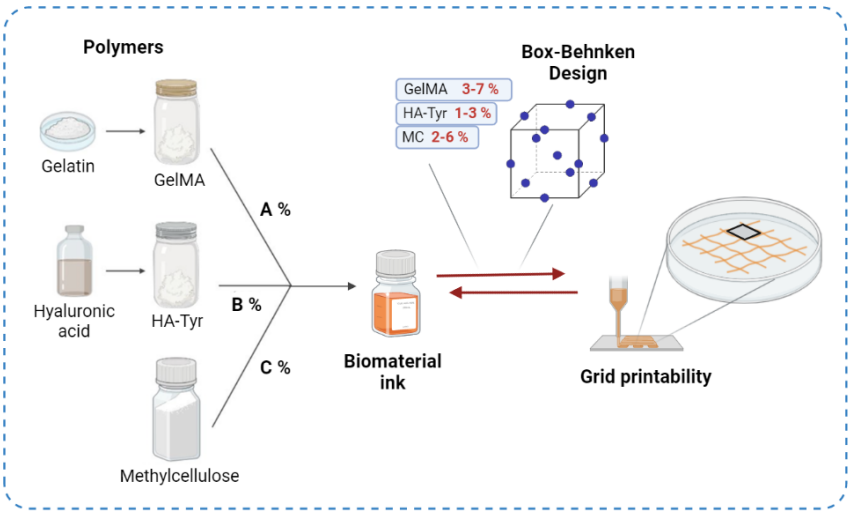

Figure 1 Schematic illustration of the employed design of experiment approach used to optimize ink composition with the ranges of design variables used in the Box–Behnken design. Created in Biorender.com

Having specified the ranges of the process variables based on our previous studies and literature reports [12, 30], values were coded as Equation 5 denotes, to aid statistical calculations (Table 1).

$$X_i = \frac{X_i - X_0}{\Delta X} \cdot 100\% \qquad (Eq.5)$$

where X_i is the coded value of the process variable; X_j is the process variable's actual value; X_0 -the actual value of X_i at the center point with the step change value denoted as ΔX.

Table 1 Values of the design variables investigated to determine printability (P_g) and their corresponding coded levels according to Box–Behnken design method

Levels	**Low**	**Center**	**High**
	-1	0	+1
GelMA [%]	3	5	7
HA-Tyr [%]	1	2	3
MC [%]	2	4	6

For each of the formulations, we printed a 20 x 20 mm grid containing 16 smaller squares (25G nozzle, speed 6 mm/s, pressure ~ 80 kPa). All prints were photographed with a scale bar and the perimeters of three different inner squares (n=3) were measured using ImageJ (NIH, USA) [31]. Gathered values were used to quantitively determine printability - P_g, based on the circularity of the pores inside of a grid [20], employing Equation 6.

$$P_g = \frac{L^2}{16A_t} \cdot 100\% \qquad (Eq.6)$$

Where L [mm] is the perimeter of the square inside of a printed grid and A_t [mm^2] corresponds to the theoretical area of the square inside of a printed grid. Ideally, P_g =100 %, indicating perfectly square-shaped pores [20, 32]. Based on the data from the experimental design, an empirical relation between printability (P_g) and the process variables was developed. The generated function was of the second-order polynomial form (Equation 7).

$$P_g = X_0 + \sum_{i=1}^{3} b_i X_i + \sum_{i=1}^{3} b_{ii} X_i^2 + \sum_{i=1}^{3} \sum_{j=1} b_{ij} X_i X_j \qquad (Eq.7)$$

Where P_g corresponds to printability, X_0 denotes the model intercept, Xi, (X_j) stands for ith (jth) system variable (GelMA, HA-Tyr, MC concentrations) and b_i, b_{ii}, b_{ij} as regression coefficients of the model.

2.6. Characterization of the ink and hydrogel

2.6.1. Rheological properties

The rheological measurements of inks and hydrogel samples were performed using a rheometer (Anton Paar MRC 302, Graz, Austria) equipped with a plate–plate geometry (25 mm). Details of the measurement are presented in S1.2.

2.6.2. Swelling, degradation and morphological properties

For swelling and degradation measurements, hydrogels prepared in the form of cylindrical discs were freeze-dried, weighted, and immediately immersed in DMEM in a sealed 24-well plate, at 37 °C. The specimens' weight directly after preparation corresponds to the time point 0 h. Next, samples were incubated in 4 mL of DMEM for 15 min, 30 min, 1 h, 2 h, 4 h, 6 h, 8 h and 24 h. After the defined time, samples were removed from the flask, excess DMEM was carefully drained with a paper towel, and hydrogel weight was recorded [30, 33]. The swelling ratio (%) and remaining mass (%) were calculated from Equations 8 and 9.

$$Swelling\ ratio\ (\%) = \frac{(m_{wet} - m_{dry})}{m_{dry}} \cdot 100\% \qquad (Eq.8)$$

Where, m_{dry} [g] is a mass of dry hydrogel, m_{wet} [g] mass of a wet hydrogel.

$$Remaining\ mass\ (\%) = \left(\frac{m_{dayn}}{m_{day0}}\right) \cdot 100\% \qquad (Eq.9)$$

Where, m_{dayn} [g] is a mass of dry hydrogel at day n, m_{day0} [g] mass of a dry hydrogel at day 0.

The microstructure of the hydrogels and their external porosity was evaluated by a scanning electron microscope (SEM) (Hitachi SU-70, Tokyo, Japan). Cylindrical-shaped hydrogel specimens were 3D printed, followed by lyophilization [30]. The freeze-dried samples were cut in half to show the cross-section and coated with platinum prior to placing them in the SEM chamber.

2.6.3. Compressive mechanical measurements

Mechanical properties were evaluated with a dynamical mechanical testing machine Shimadzu AGS-X (Kyoto, Japan) with a load cell of 20 N, additional information is presented in S1.2.

2.6.4. Cell culturing, viability and staining

NS-SV-AC cells were grown and passaged twice a week as previously described [34] using DMEM-HamF12 medium containing 5% heat-inactivated fetal bovine serum, 100 UI/mL streptomycin-penicillin and 4 mM glutamine (Thermo-Fisher Scientific). HA-Tyr, GelMA and MC powders were sterilized with UV light for 1 h prior to reconstitution in sterile DMEM-HamF12. All other solutions involved in ink formulation were sterile filtered (0.22 μm). Hydrogels were formed *in situ* in the wells of a 96-well plate or printed as 2-layer squares (4 x 4 mm) in 8-well plates and followed by cell seeding on the surface. Printed samples were sterilized in 70 % ethanol for 1h, washed thrice with PBS and incubated for one day with cell culture media prior cell seeding. The next day cells were seeded into the 96 well or 8 well plates, on the surface of hydrogels, at a density of ~1.2×10^4 cells/cm^2.

Then, cell culture media was added to each well and plates were transferred to a cell incubator (37 °C, 5 wt.% CO_2). The medium was changed every day.

We have used salivary gland NS-SV-AC cells as a soft tissue representative to determine the cell viability using MTS assay (CellTiter 96® AQueous One Solution Cell Proliferation Assay, Promega, Madison, WI, USA). We also investigated the distribution of the cells on the prepared hydrogel specimens using the LIVE/DEAD staining (Sigma Aldrich, USA). Details of cell viability evaluation and cell staining protocol are presented in S1.2.

2.6.5. Hydrogel scaffold subcutaneous implantation in rat model

Female Wistar rats (13 weeks old; 3 animals) were used for this study. Animal welfare and experimental procedures followed the EU Directive 2010/63 for animal experiments. All experimental procedures were approved by the Ethical Committee of the Grigore T. Popa University of Medicine and Pharmacy of Iasi (agreement No. 83/25.05.2021) and performed according to the EU Directive 2010/63 guidelines (The experimental details are presented in S1.2)

2.6.6. Hydrogel implantation in chick chorioallantoic membrane (CAM)

The chorioallantoic membrane (CAM) assay was used as a screening tool for the cytocompatibility and angiogenic properties of newly developed hydrogel material (The experimental details are presented in S1.2)

2.7. Statistical analysis

Data is represented by mean ± standard deviation (SD) from three independent measurements, if not otherwise mentioned. Statistic evaluation was performed with OriginPro 9.7 software, comparing multiple groups using two-way ANOVA with a Tukey

post hoc test. Significant differences are marked as follows: *($p < 0.05$) or declared as non-significant (NS) at $p > 0.05$.

3. Results and discussion

3.1. Material characterization

The introduction of phenol groups to the HA backbone (HA-Tyr) stimulates gel formation via enzymatic [35] or photocrosslinking mechanisms [15]. Similarly, for GelMA, methacryloyl residues enable photocrosslinking leading to covalent and temperature-irreversible gelation in the presence of a photoinitiation system [12, 13].

1H NMR for modified gelatin and HA has proven the successful modification of the polymers (Figure 2A, B). Characteristic peaks at δ = 5–6 ppm correspond to the presence of acrylic protons of methacryloyl of lysine and hydroxyl lysine (Figure 2C, a+b). The peak displayed at ~1.8 ppm came from the methyl proton of methacryloyl grafts (Figure 2C, d) [12]. Those peaks were not present in unmodified gelatin. Additionally, we noticed a decreased free lysine signal at 3.1–3.2 ppm, confirming the reaction with MAA (Figure 2C, c) [12, 14]. The methacrylation degree of gelatin was within the range reported in previous studies and based on 1H NMR results was estimated at 56 % [12].

For the HA-Tyr, characteristic peaks at δ = 6.7–7.2 ppm, attributed to the incorporated phenol groups in the HA backbone were observed (Figure 2D, (a, b), which agrees with existing reports [26]. Moreover, due to the formation of Tyr-O-4,6-dimethoxy-1,3,5-triazine (Tyr-O-DMT) adducts on HA, a low signal at 7.37 ppm can be seen (Figure 2D c) [26]. The degree of substitution with tyramine based on 1H NMR was estimated at 3.7 %, similarly as reported previously [26].

Functional grafting of HA with Tyr was additionally proven by the formation of a gel upon HRP-mediated oxidation and by the visible light photopolymerization with RB/SPS system [15, 36]. The same photopolymerization reaction resulting in the formation of temperature stable gel confirmed gelatin methacrylation [13].

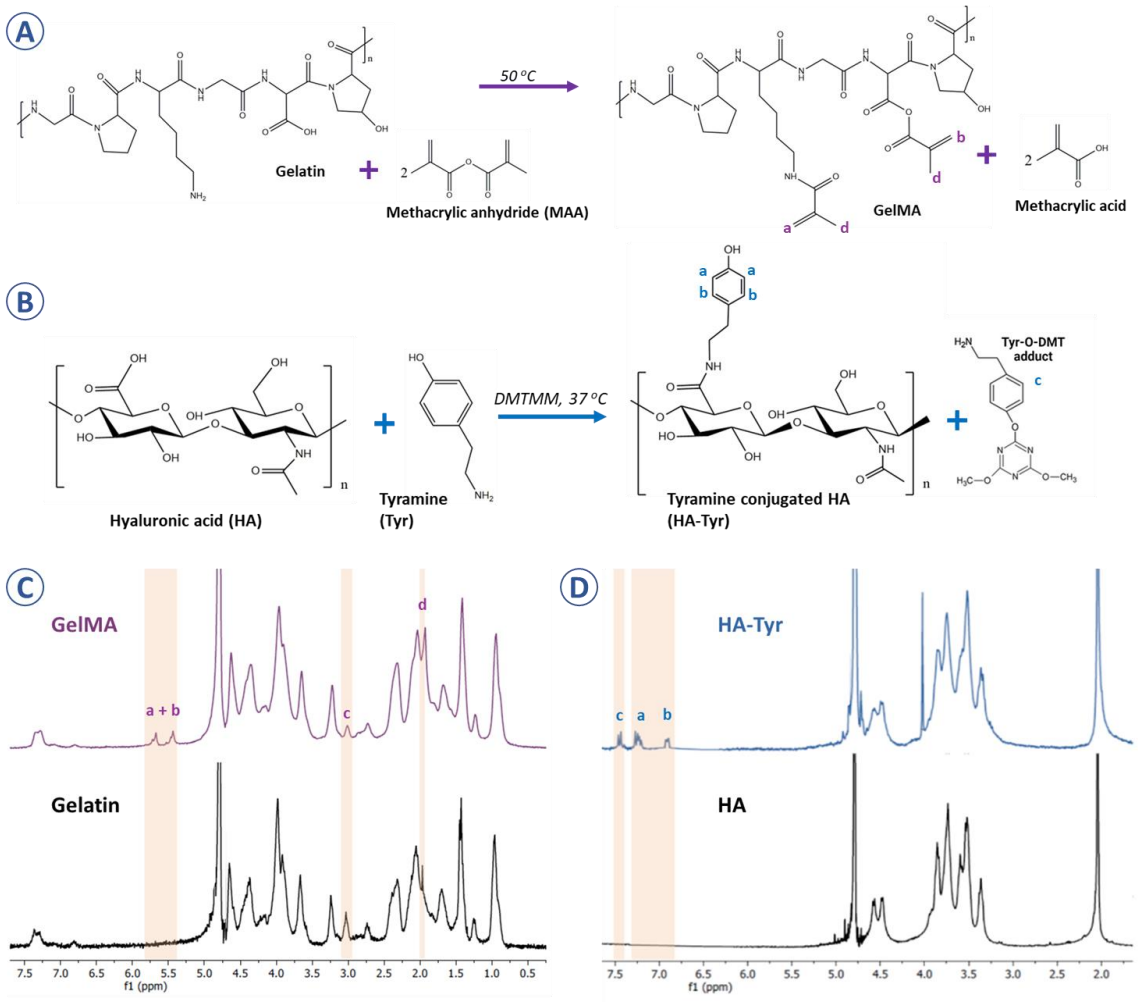

Figure 2 Reactions depicting the modification of polymers used A) methacrylation of gelatin leading to Gelatin methacryloyl (GelMA) and B) Phenolation of hyaluronic acid by conjugation with tyramine, resulting in HA-Tyr with synthesis by-product – Tyramine-O-DMT adduct [26] and corresponding nuclear magnetic resonance spectra (1H NMR) of modified (colored spectra) and non-modified (black spectra) of C) gelatin and D) hyaluronic acid

3.2. Optimisation of ink formulation

The composition of the ink greatly affects its printability. The printability of each ink formulation (identified by a unique formulation ID - #ABC, where the letters A, B, and C represent the percentage of GelMA, HA-Tyr, and MC, respectively), was measured by evaluating the printability of a 3D printed grid pattern (Table 3, Figure 3). This metric is called grid printability (P_g). The calculated P_g ranged from 6.33 % to 76.56 % (Table 3). Low MC content (2%) in the formulation resulted in no or poor printability of the inks (Figure 3). The only exception was #334 ink in which the low GelMA content and a large share of HA-Tyr translated for structural instability due to the viscosity lowering effect of HA-Tyr on the formulation. The ink formulations with high methylcellulose (MC) content (above 5%) and low hyaluronic acid-tyramine (HA-Tyr) content (1%) had the best printability of 76.04% and 76.56%. Formulations with 6% MC had a printability of over 56 %, indicating that MC is important for adjusting the printability of hydrogel materials through reversible non-polar interactions when using extrusion printing (direct ink writing) [37]. Following the grid printability P_g evaluation for each formulation a mathematical model of the relation between Pg and variables (polymers content) was established. The Equation 10 refers to a mathematical model that is used to represent the relationship between the input variables, in this case polymers and the response variable (printability) in a response surface analysis. To generate this equation, we conducted a series of experiments following the BBD as shown in Table 3 with varying levels of the input variables to collect data on the response variable. The collected data is then used to estimate the coefficients in the RSM equation using techniques such as least squares regression using Design Expert® software [22, 38]. The equation can then be used to predict the response variable for different combinations of input variables, to identify optimal operating conditions, and to analyze the effects of different variables on the response variable. Therefore, concerning our experimental study the relation between printability

and concentrations of GelMA (A), HA-Tyr (B) and MC (C) in the polymer blend can be described with Equation 10. The 3D Surface plots showing printability of the investigated ink formulations with respect to the concentration of polymers are presented in SI (Figure S.1.)

$$P_g = -161{,}84 - 11{,}54\,A + 80{,}95\,B + 57{,}36075\,C + 15{,}54\,AB - 2{,}22\,BC + 4{,}25\,A^2 - 46{,}97\,B^2 - 4{,}82\,C^2 - 4{,}66\,A^2B + 7{,}58\,AB^2 \quad \textbf{(Eq. 10)}$$

The R^2 value for the obtained model (0.9979) suggests that the employed regression model describes well the experimental results. F-value of 194.62 implies the high statistical significance of the model (Table 2). Insignificant model terms were omitted in the model description due to their negligible impact on the final model equation.

Table 2 Analysis of variance (ANOVA) for the empirical model of the Printability (P_g)

Source	Sum of Squares	Degrees of freedom	Mean Square	F-value	p-value	Remarks
Model	12153.68	10	1215.37	194.62	< 0.0001	significant
A-GelMA	11.07	1	11.07	1.77	0.2539	
B-HA-Tyr	35.40	1	35.40	5.67	0.0759	
C-MC	6591.36	1	6591.36	1055.50	< 0.0001	
AB	8.60	1	8.60	1.38	0.3057	
BC	78.77	1	78.77	12.61	0.0238	
A^2	1518.47	1	1518.47	243.16	< 0.0001	
B^2	303.20	1	303.20	48.55	0.0022	
C^2	1373.30	1	1373.30	219.91	0.0001	
A^2B	694.88	1	694.88	111.27	0.0005	
AB^2	459.88	1	459.88	73.64	0.0010	
Residual	24.98	4	6.24			
Lack of Fit	19.89	2	9.94	3.91	0.2038	not significant
Pure Error	5.09	2	2.55			
Cor Total	12178.66	14				

The high content of HA resulted in thick suspensions with poor uniformity due to the presence of tyramine residues that readily formed covalent crosslinks and caused formulation hardening impairing the extrusion process (Figure 3A and Table 3) [39]. The change in GelMA content could cause a change in printability from ~45 % to ~70 % (Figure 3B). Low concentrations of GelMA resulted in insufficiency of tyramine crosslinks to stabilize the formulation, even at low printing pressures of 20-30 kPa. MC plays a significant role in the good printability performance of the material, the printability changes from around 20% to around 80% for low and high MC share - Figure 3B. The printability of the inks can be attributed to the "chemically neutral" MC, which creates an interpenetrating network with "actively" acting polymers that strengthen the structure upon gelation [40].

It was previously reported that GelMA-based inks are characterized by low printability, even at high (>10 % w/v) concentrations [21]. The tunability of inks for extrusion bioprinting might be achieved by the addition of methylcellulose [40, 41]. Even though MC alone can help to increase the print accuracy, it does not provide enough rigidity to preserve the shape of a 3D printed structure. For this reason, MC is often blended with other polymers to increase structural stability [42, 43].

Table 3 Grid printability (P_g) at different process variable conditions – different polymer concentrations. Independent effects of the process variables (polymers concentration) on printability

N	**Formulation ID**	**Actual values of the parameters**			**Response**	**Standard deviation of Pg**
		GelMA [%]	HA-Tyr [%]	MC [%]	Pg [%]	[%]
1	#314	3	1	4	46.63	1.13
2	#512	5	1	2	11.86	3.28
3	#516	5	1	6	76.04	0.32
4	#714	7	1	4	76.56	0.27
5	#322	3	2	2	0.00*	-

6	#326	3	2	6	62.84	1.08
7	#524	5	2	4	70.37	0.33
8	#524	5	2	4	67.48	1.26
9	#524	5	2	4	70.11	0.89
10	#722	7	2	2	0.00*	-
11	#726	7	2	6	56.18	1.67
12	#334	3	3	4	6.33	4.57
13	#532	5	3	2	14.78	4.38
14	#536	5	3	6	61.21	1.93
15	#734	7	3	4	30.40	2.71

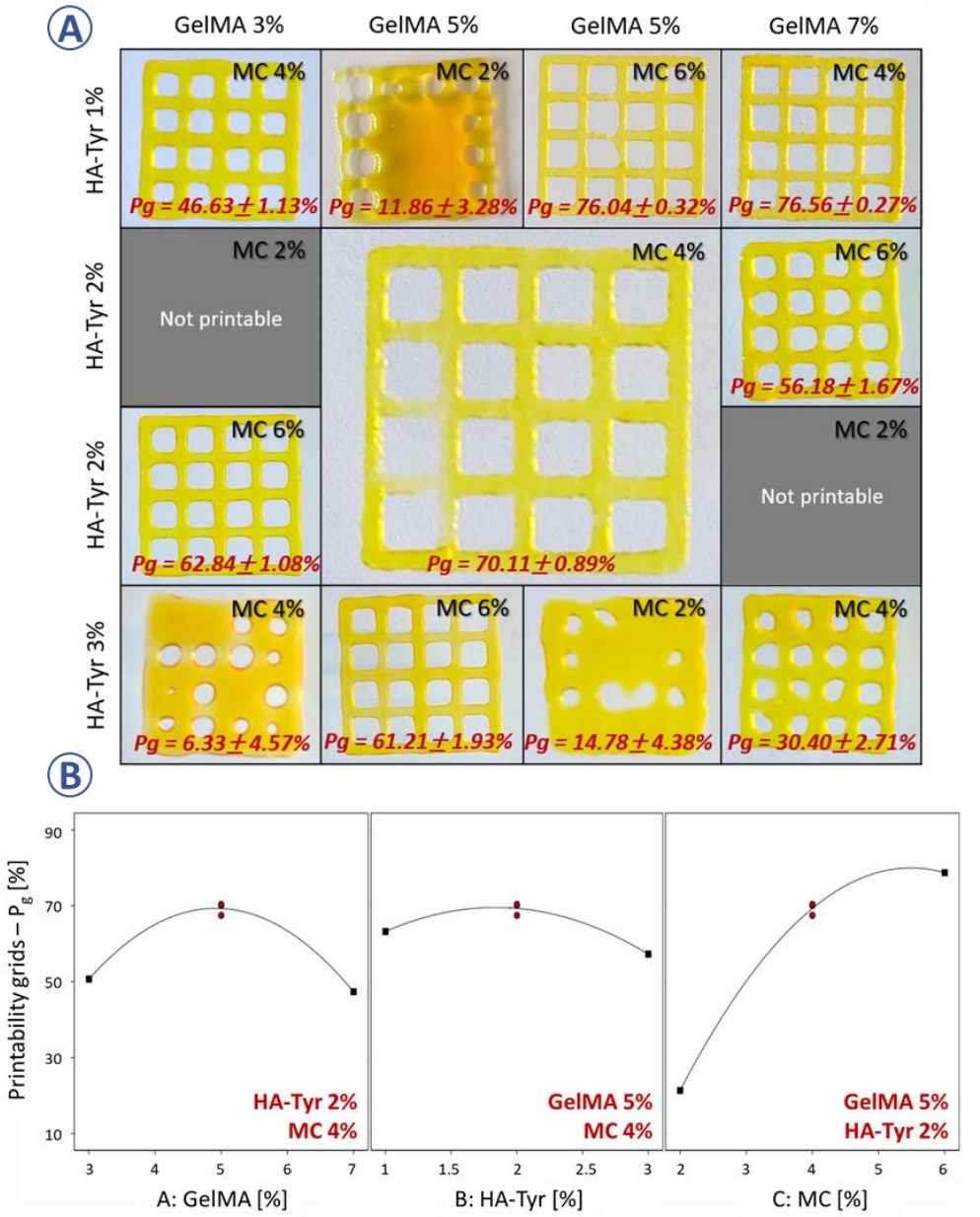

*Figure 3 A) Evaluation of the inks' printability using the grid model - Examples of the printed grids using different ink formulations, B) Effect of the variation of GelMA, HA-Tyr and MC content [%] on printability. While investigating the change of one variable the two others were held constant at the center-point values * Printability could not be determined for two of the formulations due to low shape fidelity (P_g = 0,00 %)*

The best predicted printability of 86.75 % was obtained for ink with 6.0 % GelMA, 1.2 % HA-Tyr and 5.4 % MC, which was experimentally verified to be 87.27 % (Table 3).

Table 4 Predicted and experimentally determined printability – P_g for the biomaterial ink formulation containing 6.0 % GelMA, 1.2 % HA-Tyr and 5.4% MC

Predicted P_g [%]	**Experimental P_g [%]**	**Relative absolute deviation**
86.75	87.27 ± 1.34	<0.01

In the second step, we evaluated the effect of printing parameters on ink performance described by POI (Equation 2, Figure 4A, B) [21, 29]. Various printing conditions translated differently for the values of POI, ranging from 0.19 to 0.46 within the tested range. Similarly to Webb B. and Doyle B. we noticed that at higher print pressures of around 100 kPa, the increase in printing speed has a greater impact on strand diameter and hence the print accuracy [28]. The lowest ranked POI was 0.18 (22G, 100 kPa, 6 mm/s), whereas the highest possible POI value of 0.46, found with the 25G nozzle at 70 kPa and 6 mm/s print speed. POI was not evaluated for the printing conditions resulting in discontinuous lines. The overall accuracy of a print decreases with increasing strand diameter. Therefore, accuracy is lower for high pressures and low printing speeds as it produces larger diameter strands.

Although the nominal diameters of the nozzles were substantially different, the resulting POI values were similar (0.18 and 0.21) indicating that the theoretical shear stress in a 27G

nozzle is so high that even a less precise print achieved with a 22G nozzle results in a higher POI.

Higher printing pressure results in lower POI due to compromised strand resolution and elevated shear stress levels in the nozzle. For instance, printing with 25G, 100 kPa, and 5mm/s results in a POI of 0.19 compared to 25G, 70 kPa, and 5mm/s which has a POI of 0.43 (Figure 4A). Increasing printing speed improves print accuracy as measured by POI under various conditions such as nozzle size, pressure, and speed (Figure 5B). For example, POI value increased from 0.43 to 0.46 when the printing speed increased from 5mm/s to 6mm/s, while using a smaller nozzle size like 27G didn't significantly affect POI because the increase in theoretical shear stress counterbalanced the effect of the smaller nozzle.

We developed a composite biomaterial (GelMA/HA-Tyr/MC) by optimizing the ink formulation and investigating POI to combine the biocompatible properties of HA and gelatin with the shear-thinning properties of MC. The optimal ink formulation (GelMA – 6%, HA-Tyr – 1.2%, MC – 5.4%) resulted in a printable scaffold with high flexibility and structural shape preservation. Figure 4B shows photos of a printed cuboid scaffold.

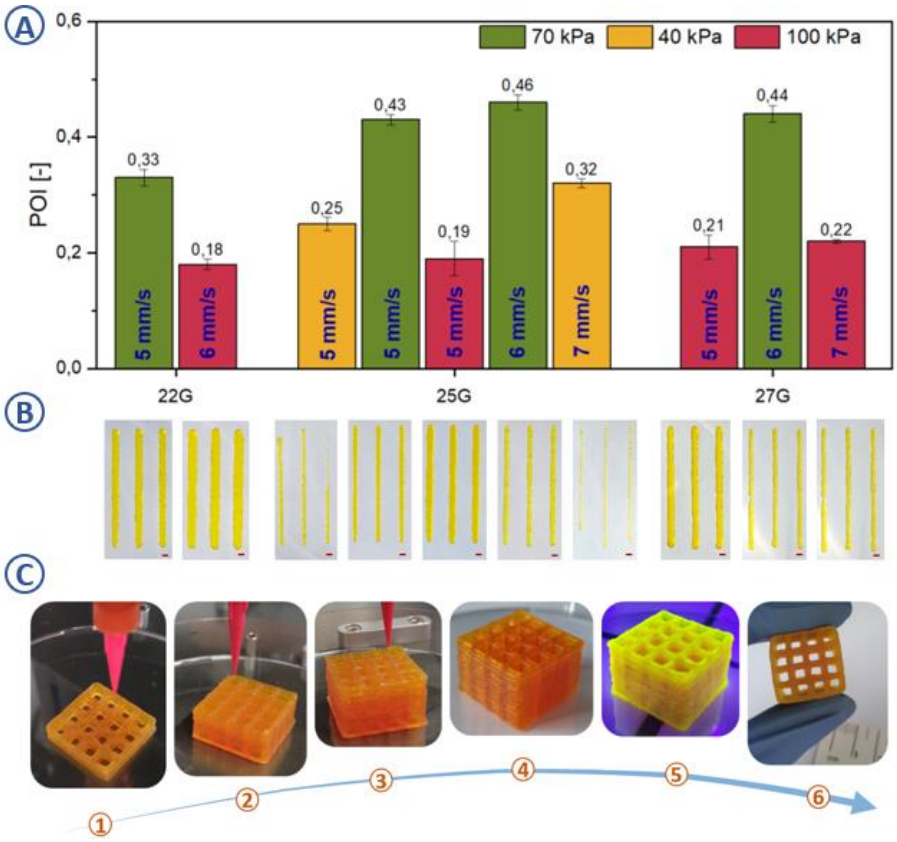

Figure 4 A) Values of POI obtained for optimized formulation, when defined conditions of printing speed, pressure and nozzle size were applied, d*ata are expressed as mean ± SD (standard deviation), based on 3 experiments, B) 3D printed linear structures used for POI determination for different printing conditions, C) Printing process of 20 x 20 x 20 mm cube, followed by crosslinking allowing to obtain a stable scaffold (subsequent stages of the 3D printing process are shown from left to right with numbers from 1 to 6)*

3.3. Ink and hydrogel rheological characterization

A relationship between rheological characteristics and printability can be established by studying material behavior under shear stress conditions [21]. Even though viscosity is often considered as a single factor affecting the extrudability of ink, it is worth investigating storage modulus (G′) and loss modulus (G″) and hence the complex viscosity of the material. In a study by Gao et all. G′ and the G″ were assumed to be the two independent variables as predictors of the required extrusion pressure and further printability. The results showed that printability and specifically the extrusion behavior is

co-determined by G′ and G″. Complex viscosity provides therefore a more comprehensive understanding of the material's rheological behavior. Flow measurements only provide information about the viscosity at a specific shear rate, whereas complex viscosity takes into account both the viscous and elastic properties of the material [44]. Additionally, complex viscosity allows for the determination of zero complex viscosity, which is a crucial parameter for printability and indicates the material's ability to spread evenly and smoothly during printing processes as it is related to the width of the transition region between Newtonian and power-law behavior [45]. Nevertheless, it was pointed previously that complex viscosity itself may fail to be a screening method for printability [46]. Similarly, within our study the complex viscosity profile of formulations #714, #734, #536, #524, and #334 closely resembled the optimized ink formulation (Figure 5A, enzymatic crosslinking), but half of them failed the grid printability test indicating that complex viscosity may be useful but not sufficient to predict printability [46].

Similarly, within our study the complex viscosity profile of formulations #714, #734, #536, #524, and #334 closely resembled the optimized ink formulation (Figure 5A, enzymatic crosslinking), but half of them failed the grid printability test indicating that complex viscosity may be useful but not sufficient to predict printability. For example, formulation #516, with a high grid printability of 76.04±0.32 %, exhibited a low viscosity profile. High viscosity does not always equate to improved mechanical strength or printing accuracy [47]. Therefore, it is crucial to examine the relationship between polymer concentrations, printability, and rheology, with a focus on shear strain sweep behavior in oscillatory tests and its interaction with shear stress forces during extrusion printing [47]. Concerning those aspects, the loss tangent can be a parameter worth investigating. The loss tangent, so the ratio of storage modulus (G′) and loss modulus (G″) of the material is an important parameter for evaluating materials’ printability as it refers to both viscous and elastic

behavior [46]. The two ink formulations #516 and #714 with the highest grid printability of 76.04±0.32 % and 76.56±0.27 % respectively had loss tangent values (0.38±0.06 and 0.37±0.03) while the optimum formulations had a loss tangent of 0.38±0.03 (Figure 5B, red line). These loss tangent results prove the close printability dependence on the loss tangent which is promising for prescreening ink printability. When juxtaposing the grid printability results with the obtained loss tangent values it was observed that formulations with grid printability higher than 60% had tangent values within for the range for the optimal ink formulation (0.3 to 0.5, denoted by green lines in Figure 5B).

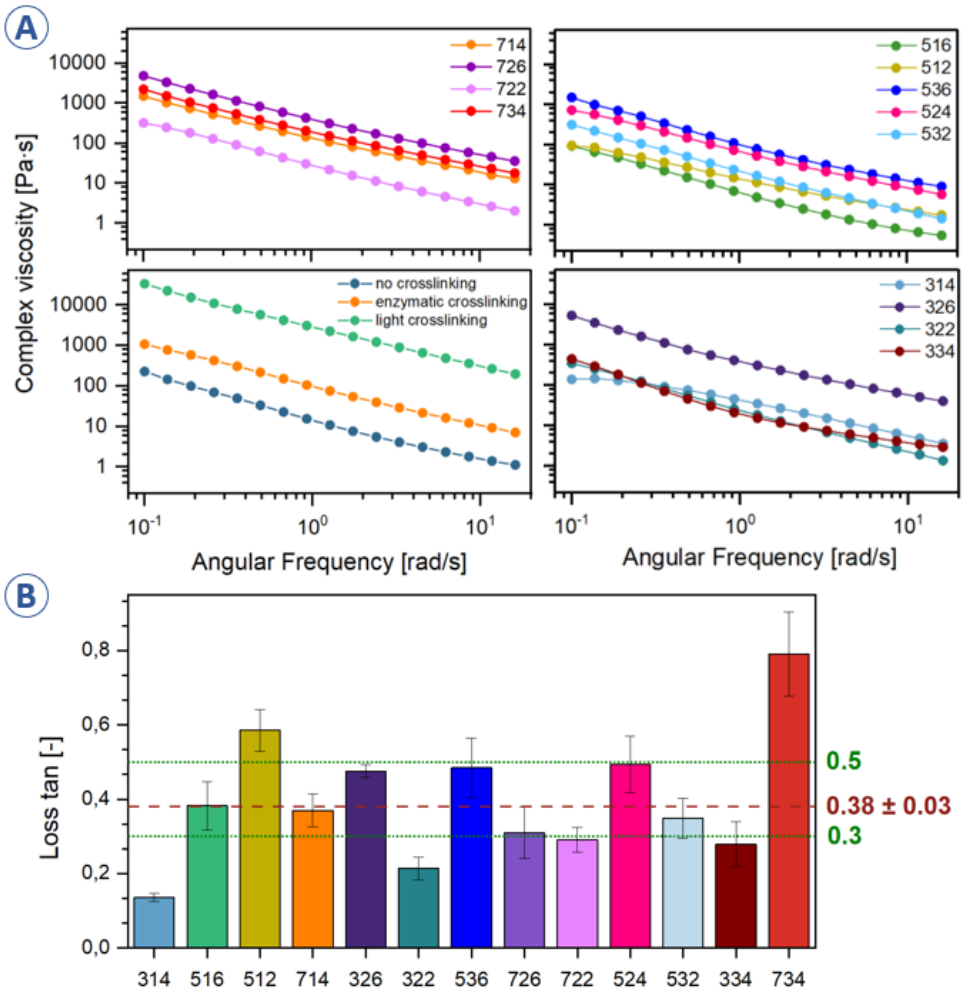

Figure 5 A) Complex viscosity graphs for the formulations described in the experimental design along with graph for optimized formulation at different stages of the crosslinking, B) Loss tangent values for tested ink formulations. The Red dashed line corresponds to the value for optimized formulation while green lines

show the range of loss tangent values for formulations whose printability exceeded 60 %. Data are expressed as mean ± SD of 3 experiments.

The crosslinking density is crucial for achieving good printing resolution and preserving structural integrity during 3D printing [48]. Although high viscosity inks are generally desirable, they require higher extrusion forces which can damage cells in bioinks [47, 49]. A reduced degree of crosslinking can make the bioink less viscous but harder to print due to faster flow. However, increasing crosslinking density can make the structure stiffer and hinder printability, so a balance must be considered [50]. Figure 6A and B demonstrate that enzymatic crosslinking or light-induced chain polymerization can increase crosslinking density and form strong covalent bonds in the material, transforming the ink into a gel [51].

Enzymatic crosslinking increased crosslinking density from 0.005 to 0.03 mol/m3 (Figure 6B), reducing elastically active junction points and elevating viscosity for better printability. Light-mediated crosslinking of HA-Tyr and GelMA further increased crosslinking density (1.1 mol/m3) and formed strong covalent bonds, resulting in a stable hydrogel with high structural integrity.

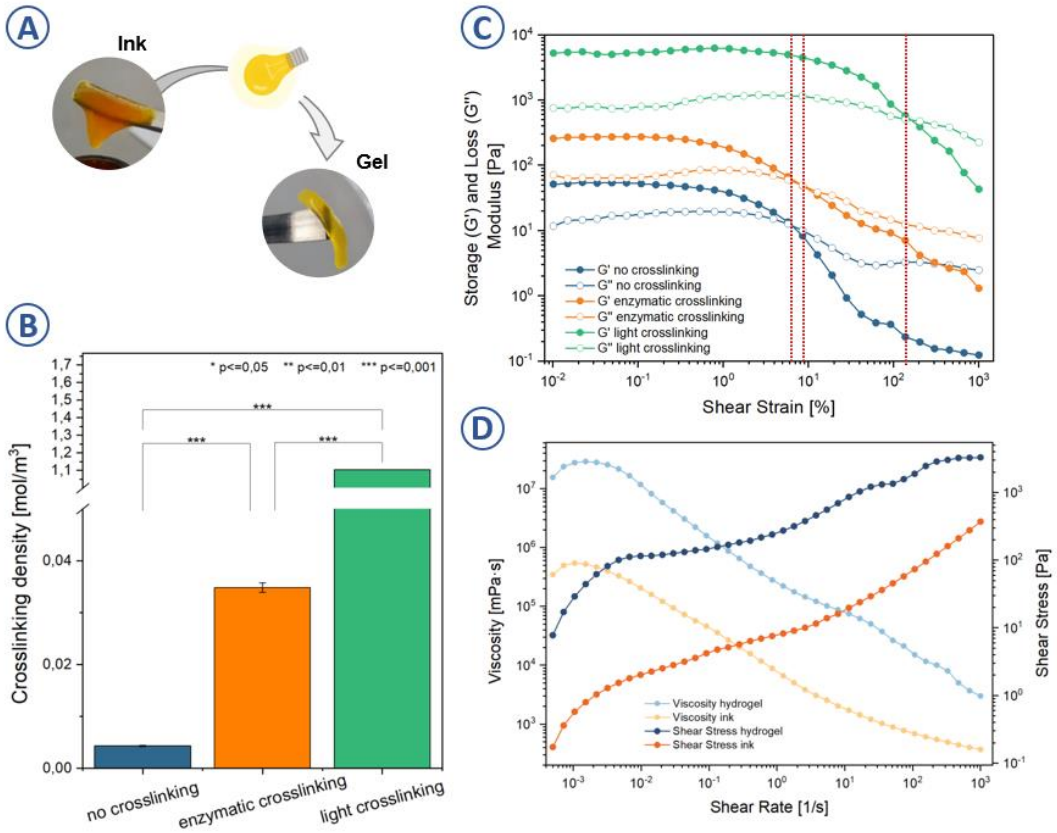

Figure 6 A) Light-induced transformation of ink to stable hydrogel, B) Crosslinking density of the structure based on frequency sweep tests, data are expressed as mean ± SD (standard deviation), based on 3 experiments, C) Amplitude sweep tests for the sample at different stages of crosslinking, D) Viscosity and flow curves (shear rate shear stress relation) for ink and hydrogel. Data are expressed as mean ± SD of X experiments.

A contractual gel to liquid transition – flow point understood as loss of the structural integrity of the material (as the viscus behavior starts to dominate over the elastic one), and the start of flow can be observed from shear strain tests, which characterize the material's response to a specific deformation under shear stress [16, 17]. In our study, we used shear strain tests to investigate the material's behavior under shear stress and found that the flow point is shifted when crosslinking steps are applied, making the material less prone to integrity loss, and inducing flow at higher shear stress values.

The storage modulus (G') values in the amplitude sweep test (Figure 6C) remained higher than the loss modulus (G"), indicating an elastic behavior of the hydrogel material regardless of crosslinking. The hydrogel required a significantly higher shear strain value to flow, indicating a higher crosslinking density.

Non-crosslinked samples required less than 7% shear strain for this transition, while pre-crosslinked samples required slightly more (10%) and light-cured samples required over 120%. Figure 6D shows that the ink's viscosity decreases as the shear rate increases, due to the cleavage of hydrogen bonds and separation of polymeric particles under the applied stress. Dropping viscosity with increasing shear rate can reaffirm the shear thinning of the ink and the ability of extrusion at low pressures as approximately 100 kPa [47, 49]. The same trend proving material flowability can be noticed in flow curves (Figure 7D) where increasing shear rate causes the increase of shear stress. This dependency changes from exponential to proportional when the shear rate exceeds 0.01 s^{-1} and again shows that light-mediated crosslinking, when applied interlocks material structure [42] and requires 10 times higher shear stress values to make the hydrogel (light-crosslinked) material flow, compared to only enzymatically crosslinked ink.

3.4. Hydrogel characterization

3.4.1. Swelling, degradation and morphological properties

The GelMA/HA-Tyr/MC hydrogel surface was smooth (Figure 7A), but its intrinsic morphology revealed open and closed pores with a diameter of 20-90 μm (Figure 7B) [30]. After 3 weeks of immersion in cell media, the pore distribution remained uniform, but the pore diameter increased to 70-300 μm (Figure 7D, E), indicating that hydrogel porosity

increases as the polymers undergo degradation, nevertheless remains stable as the hydrogels kept their original shape [48]. The efficient crosslinking provided by Rb/SPS results in a uniform internal structure that allows for greater penetration than UV-based photoinitiation systems, which can only crosslink uniformly up to a depth of 5-7 mm [52]. On the other hand, the porosity of the HA hydrogel in Figure 7C is different, with elongated pores of longitudinal shape compared to composite hydrogels containing GelMA in Figure 7B, D, E. This may be due to the lower stability of HA-only hydrogels, which collapse under their own weight.

The hydrogels degraded slowly over 3 weeks, losing 53% of their mass (Figure 7G), but maintained their shape. This suggests a uniform material that gradually releases components, providing space for cell infiltration. Figure 7D, E shows larger pores in the partially degraded sample. Chrisnandy et al. [53] emphasized the need for dually crosslinked hydrogels with a more favorable degradation scheme for cell culture application, enabling cell infiltration in the early days following implantation. Our hydrogels lost 25% of their mass in the first 4 days due to structure softening, facilitating MC leaching (Figure 7G), and slowed down to 13% over the next 11 days. Degradation processes accelerated again after the first two weeks due to residual polymer degradation and cleavage of the covalent bonds present within GelMA and HA-Tyr backbones.

The hydrogels absorbed solvent molecules, causing an increase in volume (Figure 7E), and were classified as super-absorbent hydrogels. After 8 hours, they reached an equilibrium swelling ratio of 534.9 ± 5.6%. Water absorption can be dependent on the curing time [54] and the degree of polymer modification [55], leaving a spectrum of options to tune the hydrogel swelling characteristic. 3D printed hydrogels exhibit different swelling kinetics depending on surface area, making customization of scaffold shape and porosity in 3D

printing promising for scaffold colonization by cells and accessing beneficial substances [10].

“Hydrogel porosity is an important factor for many applications, including water absorption, ease of integration with surrounding tissues, and overall strength and durability of the material [56-59]. By comparing the mechanical properties of the hydrogels fabricated by molding and 3D-printing, we aimed to investigate the effect of fabrication technique on hydrogel porosity and structure, and how this might influence their mechanical behavior. Compared to molded hydrogel samples, the 3D-printed hydrogels exhibited slightly different mechanical behavior (Figure 7I), consistent with findings reported by Sheikhi et al. [60]. The printed hydrogels had a Young's modulus of 4.4 ± 0.2 kPa and could be compressed to nearly 37% strain without fracturing. In contrast, molded hydrogels had a higher Young's modulus (7.6 ± 0.4 kPa) but cracked at 32% strain. Reported values of the Young's modulus for GelMA hydrogels ranged from 2.0 to 4.5 kPa and depended on the degree of methacrylation of GelMA [55, 61]. Study by Wu Y. et all., reports variations in values of hydrogel Young modulus in range of 3 to more than 30 kPa when GelMA concentration changed from 5% to 10% [62].

Importantly, human soft tissues such as the brain, adipose, pancreas, kidney, lungs, and salivary glands have a Young's modulus in the range of 1-10 kPa, which is comparable to the compressive modulus of our hydrogels (both molded and 3D printed) for SG tissue engineering [61]. Recent study by Otero et.all., reports similar values in range of tenths of kPa for different tissues including e.g. brain and liver [63]. The compressive strength of our hydrogels varied between the differently fabricated samples, with stress at break of 13.14 ± 0.42 kPa for printed hydrogel scaffolds and 10.51 ± 0.30 kPa for molded. This difference may be due to the presence of prone-to-compression intrinsic scaffolding in the 3D printed hydrogel, which could better transfer the force and allow for greater compression without fracturing,

while molded samples resulted in small but rapidly propagating cracks that led to faster sample failure [58, 59].

Our hydrogels had a low compressive strength and relatively low toughness (276.91 ± 23.69 kPa for printed samples and 253.35 ± 19.91 kPa for molded samples). This may be partially attributed to the MC, which had not undergone any crosslinking and therefore had not strengthened the structure [41]. The low compressive strength and toughness suggest that our scaffolds could be efficiently colonized, and the leaching processes causing the removal of MC could provide additional space for cells to proliferate. However, a higher toughness of a hydrogel could result in reduced permeability, which could hamper the hydrogel colonization processes [32].

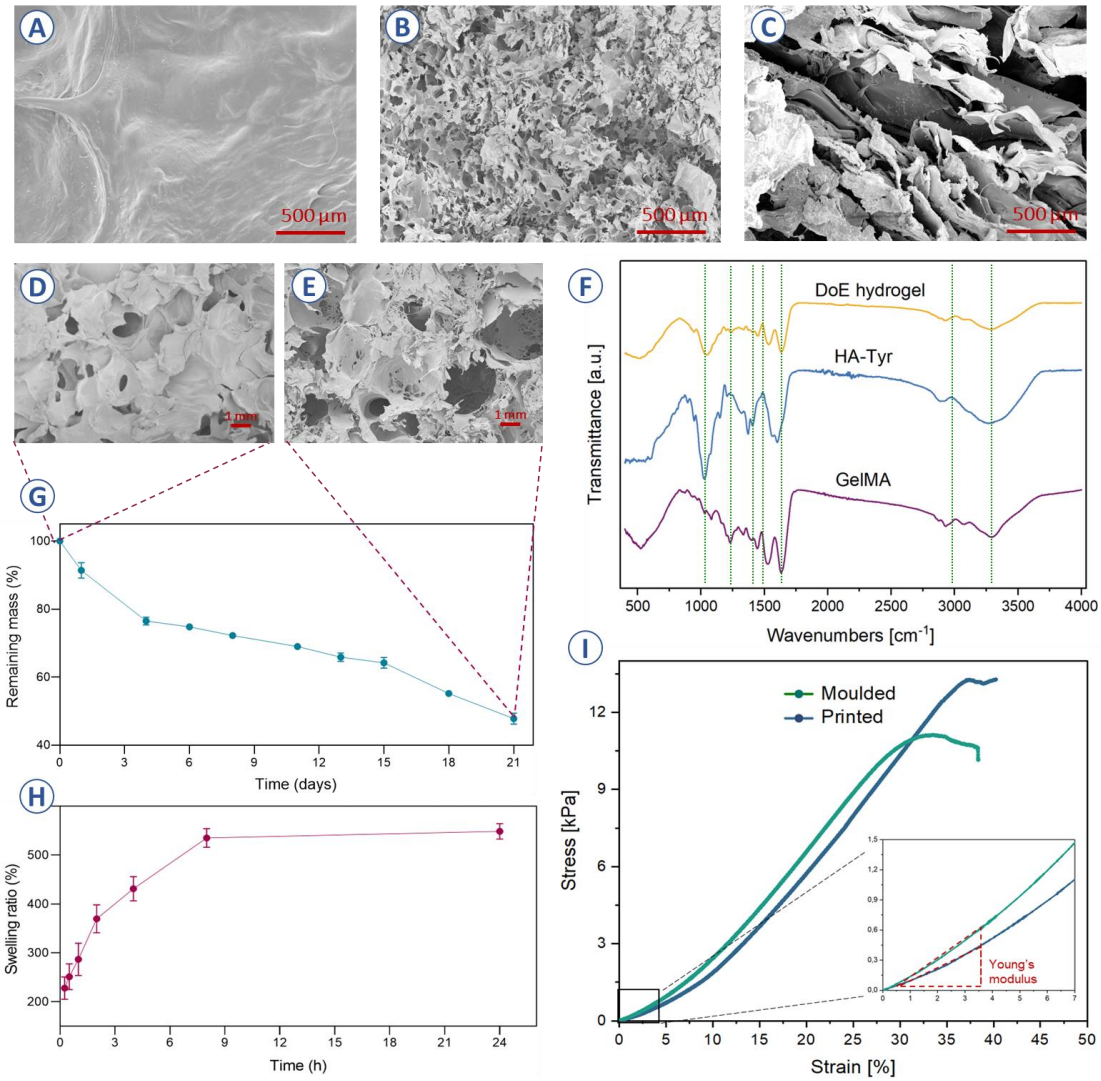

Figure 7 SEM images of DoE hydrogel samples A) surface B) cross-section C) HA-Tyr hydrogel. Cross-section of hydrogel after D) 1 day E) 3 weeks of immersion in 37 °C, in DMEM F) Fourier transform infrared (FTIR) spectra of hydrogel sample (yellow), HA-Tyr (blue), GelMA (purple) G) Swelling and H) degradation behavior of hydrogel samples in cell media (DMEM) in 37 °C I) Stress-strain curve of the hydrogel fabricated via 3D printing and molding, with the marked linear region for Young's modulus. Data are expressed as mean ± SD of 3 experiments.

ATR-IR analysis (Figure 7F) identified characteristic groups of the hydrogel and its main components participating in the crosslinking (GelMA and HA-Tyr), simultaneously confirming their presence within the hydrogel structure. The hydrogel spectrum constituted an overlap of spectra for HA-Tyr, GelMA and MC. Peaks characteristic for MC backbone,

could not be clearly identified as they remained hidden under GelMA and HA-Tyr signals, when compared with MC spectra [64]. Shifts and changes that appeared in peaks of GelMA indicate that gelatin was chemically modified to form GelMA [65]. In the spectrum of GelMA the absorption band around 3340 cm^{-1} is attributed to the O-H and N-H stretching vibrations. Stretching vibration of C-H groups can be seen as peaks in the region 2800–3100 cm^{-1}. Additionally, to the backbone structure of gelatin we may ascribe peaks at ~1650 cm^{-1}, ~1545 cm^{-1}, and ~1250 cm^{-1}, resulting from C-O stretching for amide I, N-H bending with C-H stretching for amide II and C-N stretching and N-H bending for amide III, respectively [65, 66]. The peaks around ~1250 cm^{-1} and ~1650 cm^{-1} cannot be clearly seen in hydrogel spectra due to the interactions between hydrogel components. In the spectrum of HA-Tyr a characteristic peak at ~2950 cm^{-1} proving conjugation of tyramine and presence of stretching C-H vibrations, was noted [67] in hydrogel spectra it is also present but shifted to higher wavelength number. Compared to the spectra of HA its tyramine modified derivative signals remained largely similar. We could note a broad band around ~3260 cm^{-1} resulting from the O–H groups in HA, also present in the hydrogel as an overlap of O-H stretching from both GelMA and HA-Tyr [67]. Additionally, a sharp peak at ~1040 cm^{-1} indicating the presence of pyranoid rings can be noticed in HA-Tyr which then decreases, but still may be distinguished in hydrogel spectra [68].

3.4.2. *In vitro, in vivo* and *in ovo* characterization of the hydrogel

Gelatin and its derivatives are good biomaterials for tissue regeneration due to their natural adhesion motifs and degradation processes [55, 69]. HA has also been found to promote ECM synthesis in cells [70]. In our study, we combined Gelatin and HA to make a composite cell adhesive biomaterial.

MTS assay data (Figure 8A) proven the biocompatibility of the GelMA/HA-Tyr/MC hydrogel Cell viability results for our hydrogels in every examination period were higher than reported for only HA-based hydrogels (>70 %) [15] and GelMA hydrogels (~75 %) [50]. Importantly, viability of NS-SV-AC cells remained nearly 20 % higher compared to studies employing UV crosslinking instead of visible light due to the deleterious effect of UV spectrum for cells even at short exposure times [50, 52]. Study by Lim et.all., reports high encapsulated cell viability (>80%) after 1 day of culture, for photo-initiator systems based on visible light (~450 nm), highlighting the superiority of photosystems that do not involve UV on the amount of GAGs and the capability of cells to re-differentiate [52]. It can be mostly explained by the fact that UV-light may initiate reactions with oxygen in the environment, forming reactive oxygen species (ROS), with predisposition to harm the lipid bilayer of cells [71].

When performing cell staining after 48 h, we mostly observed uniformly distributed cells or small agglomerates of which only a few cells were dead (Figure 8B). Staining results performed for cells seeded on a printed scaffold proved good cells adherence to the material, as it is possible to distinguish the scaffolds' grid [72] from an empty pore (Figure 8C). Cell adhesion is facilitated by the presence of native RGD peptides in the gelatin structure as manifested in study by Petta et.all., for HA-based gels with and without presence of RGDs [25]. Its existence in our hydrogel ensured a good microcellular environment in addition to hyaluronic acid that was able to modulate the synthesis of GAGs by the growing cells [11, 70, 73].

We noticed that NS-SV-AC cells were spreading on the hydrogel surface as was reported in different studies utilizing GelMA based hydrogels [48]. The NS-SV-AC cells' adherence to the hydrogels along with the high cell viability indicates the potential of the developed hydrogel to design a 3D model for SG.

During the *in vivo* study, none of the rats showed any signs of pain or discomfort related to the hydrogel scaffold implantation (as shown by Grimace scale and weight measurements in Figure 8J). Additionally, there were no visible signs of inflammation or infection in any of the rats. The procedure of subcutaneous implantation is depicted in Figure 8D-F. The hydrogel pouches were resected at 1 week, 2 weeks and 3 weeks after their implantation and were photographed to measure the change in scaffold dimensions (Figure 8G-I). At all-time points, healthy tissue can be observed surrounding the hydrogel with the presence of blood vessels, that are proximal or in direct contact, and the scaffolds retain their rectangular shape. The pre-implantation scaffold had an area of 25.02 ± 3.41 mm^2 (Figure 8F) and it was observed to increase as function of the implantation time in the first 2 weeks post-implantation (Figure 8K), based on the scaffold area that is visible to the naked eye on the skin. At 1-week post-implantation, the scaffold dimensions increased with approximate 19 mm^2 demonstrating an almost 79% change over the course of this time-period. The same trend was observed after 2 weeks post-implantation, when the hydrogel occupies double area (increase of nearly 108% from the initial area). Following the implantation, the area of the scaffold declined after 3 weeks to 28.12 ± 1.80 mm^2, a change of nearly 12% increase. This change in area does not appear to be the processes of degradation, rather is due to the collapse of the cell wall cavities on the perimeter of the scaffold resulting from the active movement of the rat. Active biological degradation is not expected to be possible as mammals lack the appropriate enzymes to digest the hydrogel composition.

Hydrogel cytocompatibility and angiogenic potential was further investigated by CAM assay (*in ovo* evaluation). A well-designed material for tissue regeneration purposes should easily integrate with the existing host tissue through an active blood vessel network [74-

76]. Recent studies highlight the potential of CAM assay to evidence beneficial effects of hydrogels on mechanisms guiding tissue regeneration [77].

The hydrogel samples did not have any cytotoxic effect on the blood vessel formation and embryo development within 48h of incubation. Gelatin containing materials may beneficially impact new tissue development including the process of angiogenesis [78], furthermore HA may support the synthesis of growth factors or inducing receptor interactions [73] moderating the angiogenesis process [75, 76]. If was previously reported that hydrogels can induce microvascularity in CAM models and modulate pro-angiogenic response [79]. Representative images of CAMs with hydrogel discs and control are illustrated in Figure 8L, M. Angiogenesis supporting properties of our hydrogel may be justified by a significant increase in the number of vessels branching points after 48 h of incubation compared to the control (Figure 8P). Furthermore, a slight increase was observed in the area occupied by the vessels and total vessels length after 48 h of incubation, in the presence of hydrogel (Figure 8N, O). The vessels thickness for CAMs with and without hydrogels oscillated at similar levels and was decreasing as the eggs were incubated, indicating the presence of extensive vasculogenesis and angiogenesis associated with the embryo development [80].

In vitro, in vivo, and the CAM assay showed that hydrogel may serve as a matrix supporting new vessel growth especially in the regeneration of tissues that require angiogenesis [74, 79]. When compared to the control, most of the parameters (Figure 8N-P) were not significantly different, which may assure the safety of the material and the absence of potentially carcinogenic effects, manifested by the accelerated angiogenesis [81].

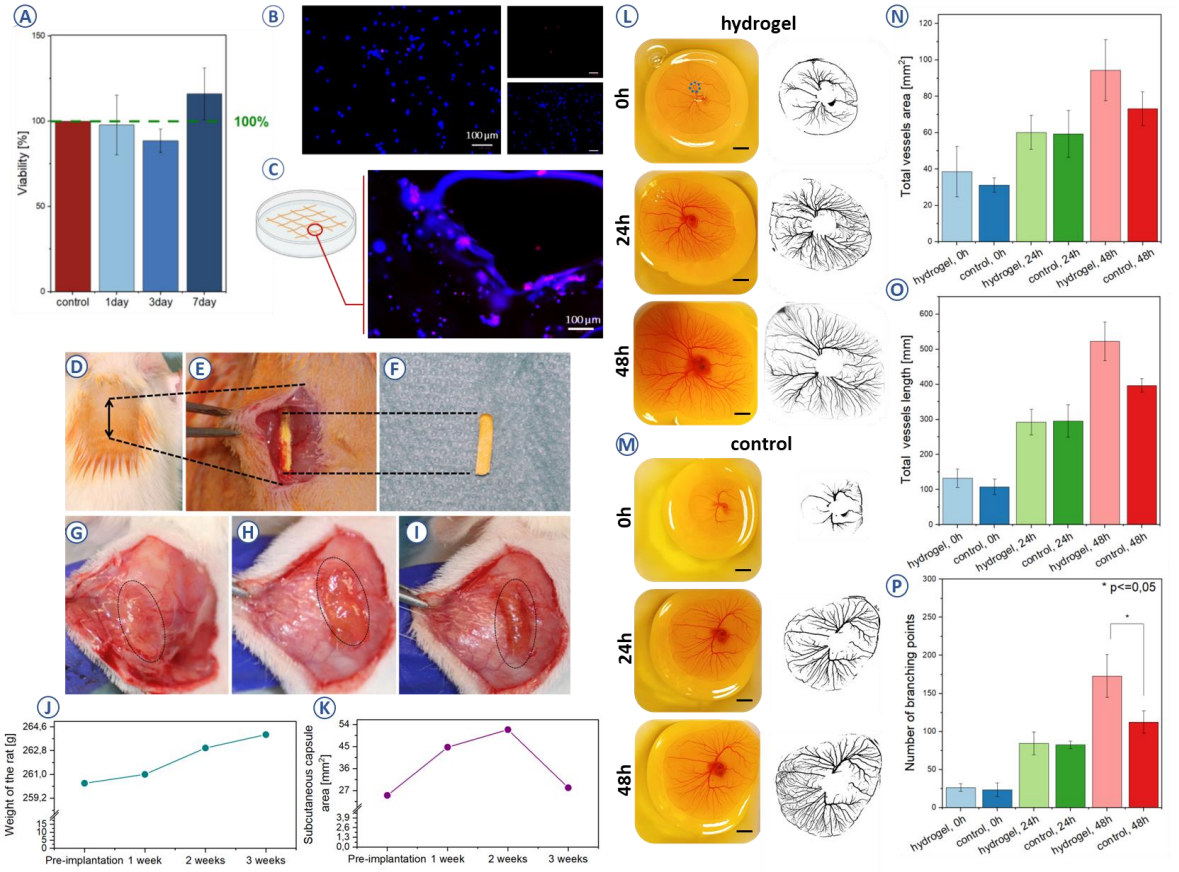

Figure 8 A) NS-SV-AC cell viability in day 1st, 3rd, 7th after seeding on the hydrogel surface, B) Staining of the cells seeded on the uniform gel surface with Hoechst (all cells) and Ethidium homodimer (dead cells) on the right separate staining results for dead cells and all cells, C) Staining of the cells adhered to the surface of the 3D printed scaffold following 48h of incubation, D) Rat skin prepared for incision, E) Hydrogel material placed subcutaneously, F) Sterilized hydrogel material prior to the implantation procedure, Capsule formed subcutaneously after: G) 1 week, H) 2 weeks, I) 3 weeks, J) Rat weight changes from pre-implantation to 3-weeks upon implantation assessed each week, K) Changes in the area of the subcutaneous capsule, formed upon implantation and assessed each week; Evaluation of the angiogenic properties of optimized hydrogel in the chick chorioallantoic membrane (CAM) assay, photos of different stages of L) material evaluation (hydrogel sample placed on vessels junction was marked with a blue circle) and M) experimental control in CAM assay (time points: 0h, 24h, 48h), first column shows photos used for vessel analysis while second shows results of the analysis as binary image from ImageJ®. Scale bars correspond to 5 mm. Quantitative evaluation of the vascular network formed in the experiment involving hydrogel and the control (without any material), N) Total vessels area, O) Total vessels length, P) Number

of branching points (data analyzed using ImageJ®). Data are expressed as mean ± SD of minimum 3 experiments.

4. Conclusions

By combining the excellent properties of gelatin, HA, and MC with extrusion-based direct printing technology, we developed a novel 3D-printable hydrogel with potential for SG tissue engineering. Thanks to the design of the experiment approach, we introduced a quantitative evaluation of printability leading to the optimisation of polymer ratios in GelMA/HA-Tyr/MC ink. This provided us with a useful set of guidelines throughout the formulation and printing process that subsequently allowed us to achieve a remarkably unique resolution of our 3D printed scaffolds. A comprehensive examination of our ink and hydrogel properties revealed that the composite materials not only presented good printability at higher polymer concentrations, but also showed mouldability when the concentration was lower. Additionally, all tested polymer blends had the ability to photocure when the RB/SPS photoinitiation system was employed, forming a stable scaffold. Cell viability studies highlighted the potential of the GelMA/HA-Tyr/MC gels to be utilized as scaffolds for tissue engineering. The hydrogels were observed to have a pro-angiogenic effect, becoming integrated into the surrounding healthy tissue and vascularized (*in vivo* study and CAM assay).

Clearly, a challenge remains in functional graft integration with targeted tissue and restoration of the structure and function. Hence, further studies are needed to probe the hydrogel's in vivo implications. In future studies we would like to investigate the differentiation of SG cells 3D plotted along with hydrogel matrix, into specific types (e.g., acinar, ductal, myoepithelial) and their arrangements into acini and ducts when provided with relevant stimulating cues.

Author Contributions

Conceptualization J.S.S, D.P., A.S., Data curation J.S.S, Formal Analysis J.S.S, F.H, G.D, I.G, F.C, Investigation J.S.S, F.H, G.D, F.C, Methodology J.S.S, D.P, A.S, C.D. Project administration A.S., Resources A.S., C.D., Supervision A.S., D.P., C.D., Validation J.S.S, A.S, L.N., Visualization J.S.S, F.H., Writing – original draft J.S.S, Writing – review & editing J.S.S, G.D, D.P, A.S, G.J, L.N, C.D.

All authors have read and agreed to the published version of the manuscript.

Funding

This research work was supported by an Aspirant fellowship from the Fonds National de la Recherche Scientific de Belgique (FNRS) (grant number 46599, 2022 awarded to Julia Simińska-Stanny).

Institutional Review Board Statement

Not applicable.

Informed Consent Statement

Not applicable.

Acknowledgments

The graphical abstract and Figure 1A were created with BioRender.com; J.S.S. gratefully acknowledge the support by a grant from the FNRS (FNRS-Aspirant, Grant No. FC 46599), F.H (Internship, Erasmus+, Code Erasmus: FPARIS481)

Conflicts of Interest

The authors declare no conflict of interest.

References

1. Adine, C. and J. Ferreira, *Bioprinting Strategies to Engineer Functional Salivary Gland Organoids*, in *Organ Tissue Engineering*. 2021. p. 173-194.
2. Hajiabbas, M., et al., *Bioengineering in salivary gland regeneration.* Journal of Biomedical Science, 2022. **29**(1): p. 35.
3. Ozdemir, T., et al., *Tuning Hydrogel Properties to Promote the Assembly of Salivary Gland Spheroids in 3D.* ACS Biomaterials Science & Engineering, 2016. **2**(12): p. 2217-2230.
4. Ozdemir, T., et al., *Biomaterials-based strategies for salivary gland tissue regeneration.* Biomater Sci, 2016. **4**(4): p. 592-604.
5. Zamboni, F., C.K. Wong, and M.N. Collins, *Hyaluronic acid association with bacterial, fungal and viral infections: Can hyaluronic acid be used as an antimicrobial polymer for biomedical and pharmaceutical applications?* Bioactive Materials, 2023. **19**: p. 458-473.
6. Trombino, S., et al., *Strategies for Hyaluronic Acid-Based Hydrogel Design in Drug Delivery.* Pharmaceutics, 2019. **11**(8).
7. Winters, C., et al., *Synthesis of conductive polymeric nanoparticles with hyaluronic acid based bioactive stabilizers for biomedical applications.* Materials Today Chemistry, 2022. **25**: p. 100969.
8. Lee, S.-w., et al., *Developmental role of hyaluronic acid and its application in salivary gland tissue engineering.* Acta Biomaterialia, 2020. **115**: p. 275-287.
9. Zamboni, F., et al., *Towards the Development of a Female Animal Model of T1DM Using Hyaluronic Acid Nanocoated Cell Transplantation: Refinements and Considerations for Future Protocols.* Pharmaceutics, 2021. **13**(11): p. 1925.
10. Poveda-Reyes, S., et al., *Gelatin-Hyaluronic Acid Hydrogels with Tuned Stiffness to Counterbalance Cellular Forces and Promote Cell Differentiation.* Macromolecular Bioscience, 2016. **16**(9): p. 1311-24.
11. Ghaffari-bohlouli, P., et al., *Printable hyaluronic acid hydrogel functionalized with yeast-derived peptide for skin wound healing.* International Journal of Biological Macromolecules, 2023. **232**: p. 123348.
12. Barroso, I.A., et al., *Photocurable GelMA Adhesives for Corneal Perforations.* Bioengineering (Basel), 2022. **9**(2).
13. Goto, R., et al., *Gelatin Methacryloyl-Riboflavin (GelMA-RF) Hydrogels for Bone Regeneration.* International journal of molecular sciences, 2021. **22**(4): p. 1635.
14. Zhu, M., et al., *Gelatin methacryloyl and its hydrogels with an exceptional degree of controllability and batch-to-batch consistency.* Scientific Reports, 2019. **9**(1): p. 6863.
15. Abdul-Monem, M.M., et al., *Light-cured hyaluronic acid composite hydrogels using riboflavin as a photoinitiator for bone regeneration applications.* Journal of Taibah University Medical Sciences, 2021. **16**(4): p. 529-539.
16. Hegab, R., et al., *Design of experiments approach to developing a robust ink for bioprinting.* Biomedical Physics & Engineering Express, 2022. **8**(3): p. 035012.
17. Piraino, L.R., D.S.W. Benoit, and L.A. DeLouise, *Optimizing Soluble Cues for Salivary Gland Tissue Mimetics Using a Design of Experiments (DoE) Approach.* Cells, 2022. **11**(12).
18. Trachtenberg, J.E., et al., *Extrusion-based 3D printing of poly(propylene fumarate) scaffolds with hydroxyapatite gradients.* J Biomater Sci Polym Ed, 2017. **28**(6): p. 532-554.
19. Pössl, A., et al., *A targeted rheological bioink development guideline and its systematic correlation with printing behavior.* Biofabrication, 2021. **13**(3).
20. Jongprasitkul, H., et al., *Two-step crosslinking to enhance the printability of methacrylated gellan gum biomaterial ink for extrusion-based 3D bioprinting.* Bioprinting, 2022. **25**: p. e00185.
21. Thattaruparambil Raveendran, N., et al., *Optimization of 3D bioprinting of periodontal ligament cells.* Dental Materials, 2019. **35**(12): p. 1683-1694.

22. Kechagias, J. and N. Vidakis, *Parametric optimization of material extrusion 3D printing process: an assessment of Box-Behnken vs. full-factorial experimental approach.* The International Journal of Advanced Manufacturing Technology, 2022. **121**: p. 1-10.
23. Salatin, S., et al., *Box-Behnken experimental design for preparation and optimization of the intranasal gels of selegiline hydrochloride.* Drug Dev Ind Pharm, 2018. **44**(10): p. 1613-1621.
24. Azuma, M., et al., *Immortalization of normal human salivary gland cells with duct-, myoepithelial-, acinar-, or squamous phenotype by transfection with SV40 ori- mutant deoxyribonucleic acid.* Labolatory Investigation 1993. **69**(1): p. 24-42.
25. Petta, D., et al., *Three-Dimensional Printing of a Tyramine Hyaluronan Derivative with Double Gelation Mechanism for Independent Tuning of Shear Thinning and Postprinting Curing.* ACS Biomaterials Science & Engineering, 2018. **4**(8): p. 3088-3098.
26. Loebel, C., et al., *Precise tailoring of tyramine-based hyaluronan hydrogel properties using DMTMM conjugation.* Carbohydrate Polymers, 2015. **115**: p. 325-333.
27. Nizioł, M., et al., *3D Printing of Thermoresponsive Hydrogel Laden with an Antimicrobial Agent towards Wound Healing Applications.* Bioengineering, 2021. **8**(6).
28. Webb, B. and B.J. Doyle, *Parameter optimization for 3D bioprinting of hydrogels.* Bioprinting, 2017. **8**: p. 8-12.
29. Hibbert, M., J.M. Viljoen, and L.H. du Plessis, *Print parameter optimisation for a Pluronic F-127 and alginate hybrid hydrogel.* Bioprinting, 2023. **30**: p. e00257.
30. Velasco-Rodriguez, B., et al., *Hybrid Methacrylated Gelatin and Hyaluronic Acid Hydrogel Scaffolds. Preparation and Systematic Characterization for Prospective Tissue Engineering Applications.* International Journal of Molecular Sciences, 2021. **22**(13): p. 6758.
31. Schneider, C.A., W.S. Rasband, and K.W. Eliceiri, *NIH Image to ImageJ: 25 years of image analysis.* Nature Methods, 2012. **9**(7): p. 671-675.
32. Naghieh, S. and X. Chen, *Printability–A key issue in extrusion-based bioprinting.* Journal of Pharmaceutical Analysis, 2021. **11**(5): p. 564-579.
33. Jafari, H., et al., *Ovarian Cell Encapsulation in an Enzymatically Crosslinked Silk-Based Hydrogel with Tunable Mechanical Properties.* Gels, 2021. **7**(3).
34. Chivasso, C., et al., *Unraveling Human AQP5-PIP Molecular Interaction and Effect on AQP5 Salivary Glands Localization in SS Patients.* Cells, 2021. **10**(8).
35. Wang, L., et al., *Dual-enzymatically crosslinked and injectable hyaluronic acid hydrogels for potential application in tissue engineering.* RSC Advances, 2020. **10**(5): p. 2870-2876.
36. Ziadlou, R., et al., *Optimization of hyaluronic acid-tyramine/silk-fibroin composite hydrogels for cartilage tissue engineering and delivery of anti-inflammatory and anabolic drugs.* Materials Science and Engineering: C, 2021. **120**: p. 111701.
37. Pepelanova, I., et al., *Gelatin-Methacryloyl (GelMA) Hydrogels with Defined Degree of Functionalization as a Versatile Toolkit for 3D Cell Culture and Extrusion Bioprinting.* Bioengineering (Basel), 2018. **5**(3).
38. Hasanzadeh, R., T. Azdast, and A. Doniavi, *Thermal Conductivity of Low-Density Polyethylene Foams Part II: Deep Investigation using Response Surface Methodology.* Journal of Thermal Science, 2020. **29**(1): p. 159-168.
39. Duan, B., et al., *3D bioprinting of heterogeneous aortic valve conduits with alginate/gelatin hydrogels.* J Biomed Mater Res A, 2013. **101**(5): p. 1255-64.
40. Simińska-Stanny, J., et al., *4D printing of patterned multimaterial magnetic hydrogel actuators.* Additive Manufacturing, 2022. **49**: p. 102506.
41. Niziol, M., et al., *3D Printing of Thermoresponsive Hydrogel Laden with an Antimicrobial Agent towards Wound Healing Applications.* Bioengineering (Basel), 2021. **8**(6).
42. Ahlfeld, T., et al., *Methylcellulose – a versatile printing material that enables biofabrication of tissue equivalents with high shape fidelity.* Biomaterials Science, 2020. **8**(8): p. 2102-2110.
43. Ahlfeld, T., et al. *A Methylcellulose Hydrogel as Support for 3D Plotting of Complex Shaped Calcium Phosphate Scaffolds*. Gels, 2018. **4**, DOI: 10.3390/gels4030068.

44. Ramli, H., et al., *Basic principle and good practices of rheology for polymers for teachers and beginners.* Chemistry Teacher International, 2022. **4**(4): p. 307-326.
45. Zare, Y., S. Park, and K.Y. Rhee, *Analysis of complex viscosity and shear thinning behavior in poly (lactic acid)/poly (ethylene oxide)/carbon nanotubes biosensor based on Carreau–Yasuda model.* Results in Physics, 2019. **13**: p. 102245.
46. Gao, T., et al., *Optimization of gelatin-alginate composite bioink printability using rheological parameters: a systematic approach.* Biofabrication, 2018. **10**(3): p. 034106.
47. Gao, T., et al., *Optimization of gelatin–alginate composite bioink printability using rheological parameters: a systematic approach.* Biofabrication, 2018. **10**(3): p. 034106.
48. Yue, K., et al., *Synthesis, properties, and biomedical applications of gelatin methacryloyl (GelMA) hydrogels.* Biomaterials, 2015. **73**: p. 254-271.
49. Hernández-Sosa, A., et al., *Optimization of the Rheological Properties of Self-Assembled Tripeptide/Alginate/Cellulose Hydrogels for 3D Printing.* Polymers, 2022. **14**(11): p. 2229.
50. GhavamiNejad, A., et al., *Crosslinking Strategies for 3D Bioprinting of Polymeric Hydrogels.* Small, 2020. **16**(35): p. 2002931.
51. Stojkov, G., et al., *Relationship between Structure and Rheology of Hydrogels for Various Applications.* Gels, 2021. **7**(4).
52. Lim, K.S., et al., *Visible Light Cross-Linking of Gelatin Hydrogels Offers an Enhanced Cell Microenvironment with Improved Light Penetration Depth.* Macromolecular Bioscience, 2019. **19**(6): p. e1900098.
53. Chrisnandy, A., et al., *Synthetic dynamic hydrogels promote degradation-independent in vitro organogenesis.* Nature Materials, 2022. **21**(4): p. 479-487.
54. Turioni, C., et al., *Biodegradable Hydrogels: Evaluation of Degradation as a Function of Synthesis Parameters and Environmental Conditions.* Soil Systems, 2021. **5**(3): p. 47.
55. Li, X., et al., *3D Culture of Chondrocytes in Gelatin Hydrogels with Different Stiffness.* Polymers (Basel), 2016. **8**(8).
56. Jiang, Z., et al., *Extrusion 3D Printing of Polymeric Materials with Advanced Properties.* Advanced Science, 2020. **7**.
57. Zhang, Z., et al., *3D Printing Super Strong Hydrogel for Artificial Meniscus.* ACS Applied Polymer Materials, 2019. **1**(8): p. 2023-2032.
58. Sartori, S., et al., *Biomimetic polyurethanes in nano and regenerative medicine.* Journal of Materials Chemistry B, 2014. **2**(32): p. 5128-5144.
59. Evans, D.W., et al., *Scale-dependent mechanical properties of native and decellularized liver tissue.* Biomechanics and Modeling in Mechanobiology, 2013. **12**(3): p. 569-580.
60. Sheikhi, M., et al., *3D printing of jammed self-supporting microgels with alternative mechanism for shape fidelity, crosslinking and conductivity.* Additive Manufacturing, 2022. **58**: p. 102997.
61. Ermis, M., *Photo-crosslinked gelatin methacrylate hydrogels with mesenchymal stem cell and endothelial cell spheroids as soft tissue substitutes.* Journal of Materials Research, 2020: p. 1-15.
62. Wu, Y., et al., *The influence of the stiffness of GelMA substrate on the outgrowth of PC12 cells.* Biosci Rep, 2019. **39**(1).
63. Tejo-Otero, A., et al., *Soft-Tissue-Mimicking Using Hydrogels for the Development of Phantoms.* Gels, 2022. **8**(1).
64. Maleky, S., et al., *Tetracycline Adsorption from Aqueous Media by Magnetically Separable Fe3O4@Methylcellulose/APTMS: Isotherm, Kinetic and Thermodynamic Studies.* Journal of Polymers and the Environment, 2022. **30**.
65. Modaresifar, K., A. Hadjizadeh, and H. Niknejad, *Design and fabrication of GelMA/chitosan nanoparticles composite hydrogel for angiogenic growth factor delivery.* Artificial Cells, Nanomedicine, and Biotechnology, 2018. **46**(8): p. 1799-1808.
66. Fonseca, D., et al., *Swellable Gelatin Methacryloyl Microneedles for Extraction of Interstitial Skin Fluid toward Minimally Invasive Monitoring of Urea.* Macromolecular Bioscience, 2020. **20**: p. 2000195.

67. Egbu, R., et al., *Antibody loaded collapsible hyaluronic acid hydrogels for intraocular delivery.* European Journal of Pharmaceutics and Biopharmaceutics, 2018. **124**: p. 95-103.
68. Mirzayeva, T., et al., *Screening of the Chemical Composition and Identification of Hyaluronic Acid in Food Supplements by Fractionation and Fourier-Transform Infrared Spectroscopy.* Polymers (Basel), 2021. **13**(22).
69. Cui, H., et al., *In vitro and in vivo evaluation of 3D bioprinted small-diameter vasculature with smooth muscle and endothelium.* Biofabrication, 2019. **12**(1): p. 015004.
70. Thanh, T.N., et al., *Hyaluronic acid crosslinked with alginate hydrogel: A versatile and biocompatible bioink platform for tissue engineering.* European Polymer Journal, 2022. **166**: p. 111027.
71. El-Beltagi, H.S., W. El-Desouky, and R.S. Yousef, *Synergistic Antioxidant Scavenging Activities of Grape Seed and Green Tea Extracts against Oxidative Stress.* Notulae Botanicae Horti Agrobotanici Cluj-Napoca, 2016. **44**(2): p. 367-374.
72. Li, H., et al., *Submerged and non-submerged 3D bioprinting approaches for the fabrication of complex structures with the hydrogel pair GelMA and alginate/methylcellulose.* Additive Manufacturing, 2021. **37**: p. 101640.
73. Park, D., et al., *Hyaluronic acid promotes angiogenesis by inducing RHAMM-TGFβ receptor interaction via CD44-PKCδ.* Molecular Cells, 2012. **33**(6): p. 563-74.
74. Jafari, H., et al., *An injectable, self-healing, 3D printable, double network co-enzymatically crosslinked hydrogel using marine poly- and oligo-saccharides for wound healing application.* Applied Materials Today, 2022. **29**: p. 101581.
75. Luo, Y., et al., *Hyaluronic Acid Facilitates Angiogenesis of Endothelial Colony Forming Cell Combining With Mesenchymal Stem Cell via CD44/ MicroRNA-139-5p Pathway.* Frontiers in Bioengineering and Biotechnology, 2022. **10**.
76. Pardue, E.L., S. Ibrahim, and A. Ramamurthi, *Role of hyaluronan in angiogenesis and its utility to angiogenic tissue engineering.* Organogenesis, 2008. **4**(4): p. 203-14.
77. Oliinyk, D., et al. *Chorioallantoic Membrane Assay at the Cross-Roads of Adipose-Tissue-Derived Stem Cell Research*. Cells, 2023. **12**, DOI: 10.3390/cells12040592.
78. Dreesmann, L., M. Ahlers, and B. Schlosshauer, *The pro-angiogenic characteristics of a cross-linked gelatin matrix.* Biomaterials, 2007. **28**(36): p. 5536-5543.
79. Kocak, F.Z., et al., *In‐Situ Forming pH and Thermosensitive Injectable Hydrogels to Stimulate Angiogenesis: Potential Candidates for Fast Bone Regeneration Applications.* International Journal of Molecular Sciences, 2020. **21**: p. 1633.
80. Merckx, G., et al., *Chorioallantoic Membrane Assay as Model for Angiogenesis in Tissue Engineering: Focus on Stem Cells.* Tissue Engineering Part B: Reviews, 2020. **26**(6): p. 519-539.
81. Eckrich, J., et al., *Monitoring of tumor growth and vascularization with repetitive ultrasonography in the chicken chorioallantoic-membrane-assay.* Scientific Reports, 2020. **10**(1): p. 18585.